Spin waves in the collinear antiferromagnetic phase of Mn_5Si_3

F. J. dos Santos,[1,2,*] N. Biniskos,[3,†] S. Raymond,[4] K. Schmalzl,[5] M. dos Santos Dias,[1] P. Steffens,[6] J. Persson,[7] S. Blügel,[1] S. Lounis,[1,8] and T. Brückel[7]

[1]*Peter Grünberg Institut and Institute for Advanced Simulations, Forschungszentrum Jülich and JARA, D-52425 Jülich, Germany*
[2]*Department of Physics, RWTH Aachen University, D-52056 Aachen, Germany*
[3]*Forschungszentrum Jülich GmbH, Jülich Centre for Neutron Science at MLZ, Lichtenbergstraße 1, D-85748 Garching, Germany*
[4]*Université Grenoble Alpes, CEA, IRIG, MEM, F-38000 Grenoble, France*
[5]*Forschungszentrum Jülich GmbH, Jülich Centre for Neutron Science at ILL, 71 avenue des Martyrs, F-38000 Grenoble, France*
[6]*Institut Laue-Langevin, 71 avenue des Martyrs, F-38000 Grenoble, France*
[7]*Forschungszentrum Jülich GmbH, Jülich Centre for Neutron Science (JCNS-2) and Peter Grünberg Institut (PGI-4), JARA-FIT, D-52425 Jülich, Germany*
[8]*Faculty of Physics, University of Duisburg-Essen, D-47053 Duisburg, Germany*

(Received 9 November 2020; accepted 17 December 2020; published 7 January 2021)

By combining two independent approaches, inelastic neutron-scattering measurements and density-functional-theory calculations, we study the spin waves in the collinear antiferromagnetic phase (AFM2) of Mn_5Si_3. We obtain its magnetic ground-state properties and electronic structure. This study allowed us to determine the dominant magnetic exchange interactions and magnetocrystalline anisotropy in the AFM2 phase of Mn_5Si_3. Moreover, the evolution of the spin excitation spectrum is investigated under the influence of an external magnetic field perpendicular to the anisotropy easy axis. The low-energy magnon modes show a different magnetic field dependence, which is a direct consequence of their different precessional nature. Finally, possible effects related to the Dzyaloshinskii-Moriya interaction are also considered.

DOI: 10.1103/PhysRevB.103.024407

I. INTRODUCTION

The study of magnetism at a microscopic level can lead to designing cutting-edge technological applications for data processing and storage, information transmission, and magnetic refrigeration. In recent years, antiferromagnetic (AFM) materials have attracted great interest in the research field of spintronics [1]. Bulk Mn_5Si_3 is an AFM intermetallic compound that hosts rich physics. Its interesting properties, such as the complex magnetic structure [2], the anomalous Hall effect [3], and the inverse magnetocaloric effect [4], have been attributed to an instability of the Mn magnetic moments. It is also worth mentioning that in nanoparticle [5] and nanowire [6] form, Mn_5Si_3 is considered to have great potential in future electronic and spintronic devices. Despite the intense research activity over the past decades [2–4,7–16], many open questions remain regarding the minimal magnetic model Hamiltonian, the role of the spin fluctuations in the magnetically ordered phases, and which Mn site is responsible for them. To address some of these questions, in the present study, we performed inelastic neutron-scattering experiments and applied first-principles calculations.

The crystal and magnetic structure of bulk Mn_5Si_3 has been established by neutron-diffraction measurements [2,7,8], and the magnetic phase diagram as a function of temperature and magnetic field has been extensively studied by magnetization and electrical transport measurements [9–12,17]. In the paramagnetic (PM) state, Mn_5Si_3 crystallizes in the hexagonal space group $P6_3/mcm$ with two distinct crystallographic positions for Mn atoms (sites Mn1 and Mn2) [7] and undergoes two successive first-order phase transitions towards antiferromagnetic phases, which occur at $T_{N_2} \approx 100$ K (AFM2) and $T_{N_1} \approx 66$ K (AFM1), respectively [17]. The electric resistivity shows a metallic behavior with two anomalies corresponding to these phase transitions [10].

At $T_{N_2} \approx 100$ K (AFM2), the crystal structure changes from hexagonal to orthorhombic with space group $Ccmm$, and Mn2 divides into two sets of inequivalent positions [8]. In the orthorhombic cell, magnetic reflections follow the condition $h + k$ odd, and the magnetic propagation vector is $\boldsymbol{\kappa} = (0, 1, 0)$. In the AFM2 phase, the Mn1 and one-third of the Mn2 atoms have no ordered moments, and the remaining Mn2 atoms have their magnetic moments of magnitude 1.48(1) μ_B aligned almost parallel and antiparallel to the b axis of the orthorhombic cell [8] [see Fig. 1(a)]. At a lower temperature, at $T_{N_1} \approx 66$ K (AFM1), a structural distortion occurs to an orthorhombic cell without inversion symmetry (space group $Cc2m$) [2]. The magnetic moments reorient in a highly noncollinear and noncoplanar arrangement, while the propagation vector remains the same. Mn1 atoms acquire a magnetic moment of magnitude 1.20(5) μ_B, and still one-third of the Mn2 atoms have no ordered moments, just as in the AFM2 phase. The rest of the Mn2 atoms carry a moment of 2.30(9) and 1.85(9) μ_B, depending on their site.

*f.dos.santos@fz-juelich.de (present address: EPFL, Route Cantonale, CH-1015 Lausanne, Switzerland; flaviano.dossantos@epfl.ch)
†n.biniskos@fz-juelich.de

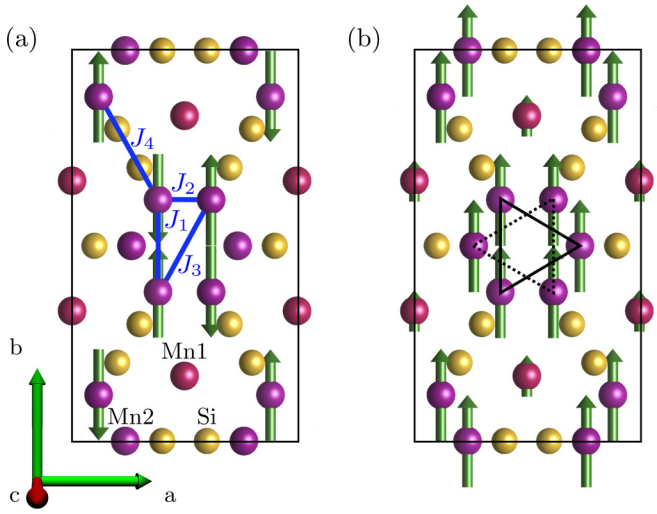

FIG. 1. (a) Projection of the structure of Mn_5Si_3 in the AFM2 phase in the *ab* plane of the orthorhombic cell according to single-crystal neutron-diffraction data [8]. The blue solid lines indicate the relevant exchange interactions used in the Heisenberg Hamiltonian. (b) Predicted metastable FM phase from first-principles calculations (see details in text). The two triangles indicate Mn2 atoms located in different planes.

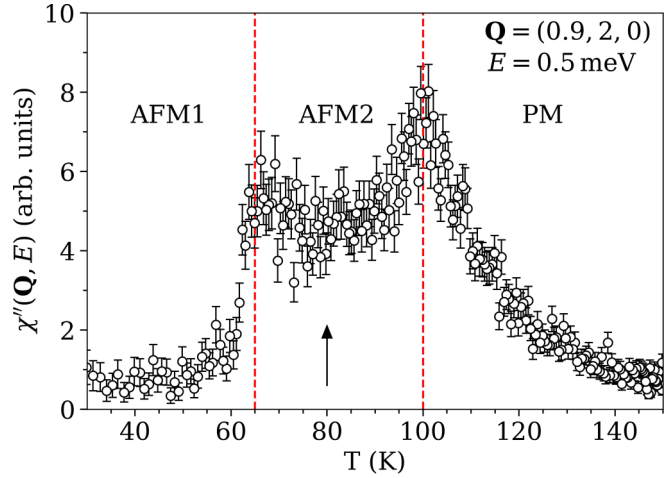

FIG. 2. Temperature dependence of the dynamical spin susceptibility $\chi''(\mathbf{Q}, E)$ of Mn_5Si_3 at $\mathbf{Q} = (0.9, 2, 0)$ and $E = 0.5$ meV measured with unpolarized neutrons with $k_f = 1.5$ Å^{-1}. The vertical red dashed lines indicate $T_{N_2} \approx 100$ K and $T_{N_1} \approx 66$ K. The arrow indicates the temperature ($T = 80$ K) where INS data were collected.

II. EXPERIMENTAL PART

A. Experimental details

The Mn_5Si_3 single crystal was grown by the Czochralski method [4]. The sample with a mass of about 7 g was mounted on an aluminum sample holder and was oriented in the [100]/[010] scattering plane of the orthorhombic symmetry. Inelastic neutron-scattering (INS) measurements were carried out on the cold triple-axis spectrometers (TASs) IN12 [18] and Three Axis Instrument for Low Energy Spectrometry (ThALES) at the Institut Laue-Langevin (ILL) in Grenoble, France. Both TASs were set up in the W configuration, and inelastic scans were performed with constant $\mathbf{k}_f$, where $\mathbf{k}_f$ is the wave vector of the scattered neutron beam.

Unpolarized INS measurements were performed at IN12, and focusing setups were employed. The spectrometer was equipped with pyrolytic graphite [PG(002)] crystals as the monochromator and analyzer, and 40'-open-open collimations were installed. Higher-order contamination was removed using a velocity selector (VS) before the monochromator and a beryllium (Be) filter in the scattered neutron beam. The sample was cooled below room temperature with a ^{4}He flow cryostat. Spin dynamics investigations with unpolarized neutrons under the magnetic field were carried out using a 10-T vertical field magnet. For these measurements, the Be filter was removed. The single crystal was cooled down from the PM state to $T = 80$ K (AFM2 phase) without the presence of an external magnetic field. The field was applied along the *c* axis of the orthorhombic symmetry of Mn_5Si_3, and the spectra were collected with increasing field strength.

With ThALES, longitudinal polarization analysis (LPA) was performed using Cryogenic Polarization Analysis Device (CRYOPAD) [19] to guide and orient the neutron beam polarization with a strictly zero magnetic field in the sample position. The TAS was equipped with polarizing Heusler [$Cu_2MnAl(111)$] crystals as the monochromator and analyzer. A flipping ratio of 14 was determined from measurements in a graphite sample. Fully focusing setups were employed, and higher-order contamination was removed using a VS and a Be filter before the monochromator and in the scattered neutron beam, respectively. Inelastic scans were performed with a constant $\mathbf{k}_f$ of 1.1 Å^{-1}. For the polarized INS experiments the common Cartesian coordinate system was used [20]: the *x* axis parallel to the scattering vector $\mathbf{Q}$ [21], the *y* axis perpendicular to $\mathbf{Q}$ in the scattering plane, and the *z* axis perpendicular to the scattering plane.

B. Unpolarized INS measurements

To determine the extent of the critical spin fluctuations related to the two AFM transitions, spectra were collected with an unpolarized neutron beam at small $\mathbf{q}$. A $(\mathbf{Q}, E)$ position was carefully selected to avoid contributions to the measured intensity from the elastic and inelastic scattering from the magnetic zone centers and low-energy magnon modes, respectively. The obtained intensity after background subtraction was corrected by the detailed balance factor so that the final result relates to the imaginary part of the dynamical spin susceptibility $\chi''(\mathbf{Q}, E)$. Figure 2 shows the extent of the spin fluctuations for $\mathbf{Q} = (0.9, 2, 0)$ and $E = 0.5$ meV in the PM state, as well as the critical fluctuations due to the two AFM phase transitions as seen by the broad tail above T_N. $\chi''(\mathbf{Q}, E)$ shows two maxima at T_{N_2} and T_{N_1}, in agreement with the established magnetic phase diagrams of Mn_5Si_3 where the AFM transitions occur [9,12].

Magnetic excitations were measured around the magnetic zone center $\mathbf{G} = (1, 2, 0)$ at $T = 80$ K, a temperature selected well inside the AFM2 phase where the intensity shows a plateau and the combined critical spin fluctuations from the PM to the AFM2 ($T_{N_2} \approx 100$ K) and from the AFM2 to the AFM1 ($T_{N_1} \approx 66$ K) transitions have minimal intensities (see

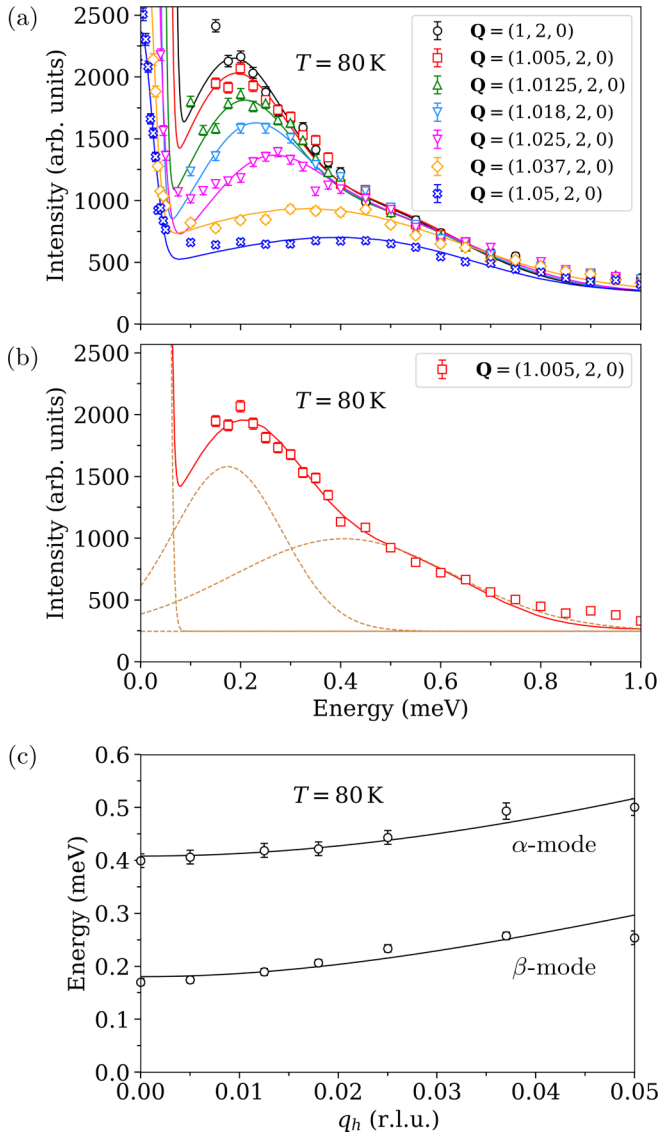

FIG. 3. (a) Energy spectra of Mn_5Si_3 at $\mathbf{Q} = (1 + q_h, 2, 0)$ measured with the IN12 spectrometer with unpolarized setup with $k_f = 1.05$ Å^{-1} at $T = 80$ K. While the two modes are unresolved at larger values of q_h, we show, using polarized neutrons, that polarization analysis resolves the peaks to $q_h = 0.06$ r.l.u. (b) Fitting of the E scan at $\mathbf{Q} = (1.005, 2, 0)$. The three dashed lines correspond to Gaussian functions sitting on top of a flat background. The solid lines indicate the overall fits as described in the text. (c) Low-energy magnon dispersion at $T = 80$ K along the $(h00)$ direction. The solid lines are fits with the empirical dispersion relation $E = \sqrt{\Delta^2 + C^2q^2}$.

Fig. 2). The energy dependence of the measured excitations at different Q_h positions is shown in Fig. 3(a), where $\mathbf{Q} = (Q_h, 2, 0)$. The individual spectra consist of three peaks. The first peak that is always centered at $E = 0$ meV corresponds to the elastic line. The two other peaks appear at finite E and shift to higher-energy transfers as Q_h increases, characteristic of dispersive spin waves. To analyze the obtained spectra, a constant background was assumed, and Gaussian functions were selected to describe the peaks. One could argue that the signal at finite E at $\mathbf{Q} = (1.037, 2, 0)$ and $\mathbf{Q} = (1.05, 2, 0)$ could be described by a single broad peak. However, the use of polarized neutrons (see Sec. II D) justifies the existence of two peaks for the excitations, since the polarized INS cross sections implore strict fitting conditions. A typical E scan collected at $\mathbf{Q} = (1.005, 2, 0)$ with the individual fit for the elastic and spin-wave signals is shown in Fig. 3(b).

The obtained low-energy experimental spin-wave dispersion along the $(h00)$ symmetry direction in the AFM2 phase of Mn_5Si_3 is shown in Fig. 3(c). There are two characteristic features: (i) There are two small energy gaps at $\mathbf{q} = 0$, and (ii) the lowest magnetic excitations can be described by the empirical dispersion relation $E = \sqrt{\Delta^2 + C^2q^2}$ [22], where Δ refers to the spin gap and C is a constant. The obtained values for the two magnon modes are as follows: $\Delta_\alpha = 0.408(7)$ meV, $C_\alpha = 6.3(5)$ meV/r.l.u., $\Delta_\beta = 0.181(4)$ meV, and $C_\beta = 4.7(3)$ meV/r.l.u. The observed gaps are indications of two easy-axis anisotropies, an assumption stemming from the collinear spin arrangement in the AFM2 phase of Mn_5Si_3. In order to describe the magnon spectrum and to extract the dominant magnetic exchange interactions and magnetocrystalline anisotropy in the AFM2 phase, theoretical calculations were employed (see Sec. III). In what follows, the modes originating from Δ_α and Δ_β will be referred to as the α and β modes, respectively.

C. Unpolarized INS measurements under a magnetic field

For $\mathbf{H} \parallel \hat{\mathbf{c}}$, neutron-diffraction measurements [13] performed in single crystals of Mn_5Si_3 indicate that no field-induced transition occurs within the AFM2 phase, and consistent with the macroscopic data [9,11,12], the PM state is not reached up to $H = 8$ T due to the steep $T_{N_2}(H)$ phase boundary. In order to investigate the magnon spectrum under a magnetic field, energy spectra were collected at three different Q_h positions (1, 1.018, and 1.025 r.l.u.) around the magnetic Bragg peak $\mathbf{G} = (1, 2, 0)$. Figure 4(a) shows such characteristic scans at $Q_h = 1$ r.l.u. for different magnetic fields. The obtained spectra were analyzed as described in the previous section. For increasing magnetic field, the two peaks that correspond to the α and β modes show different behavior. As the field increases, the position and intensity of the α mode are not significantly affected in contrast to the β mode, which disperses with the field and in which a continuous diminution of intensity is observed. It should be noted that at $H = 4$ T, the two peaks seem to merge.

The same observations regarding the behavior of the two modes stem from measurements at $Q_h = 1.018$ r.l.u. and $Q_h = 1.025$ r.l.u. and are summarized in Fig. 4(b). The obtained results indicate that the modes behave differently under the external magnetic field possibly due to their different polarization. To shed light on this behavior, spectra were collected using the polarized INS method.

D. Polarized INS measurements

As a general rule, neutron scattering is only sensitive to magnetic excitations perpendicular to $\mathbf{Q}$ [20]. With LPA it is possible to separate magnetic fluctuations polarized along different directions in spin space. The initial polarization was prepared parallel to the x axis, perpendicular to $\mathbf{Q}$ in the scattering plane (y axis), and perpendicular to the scattering

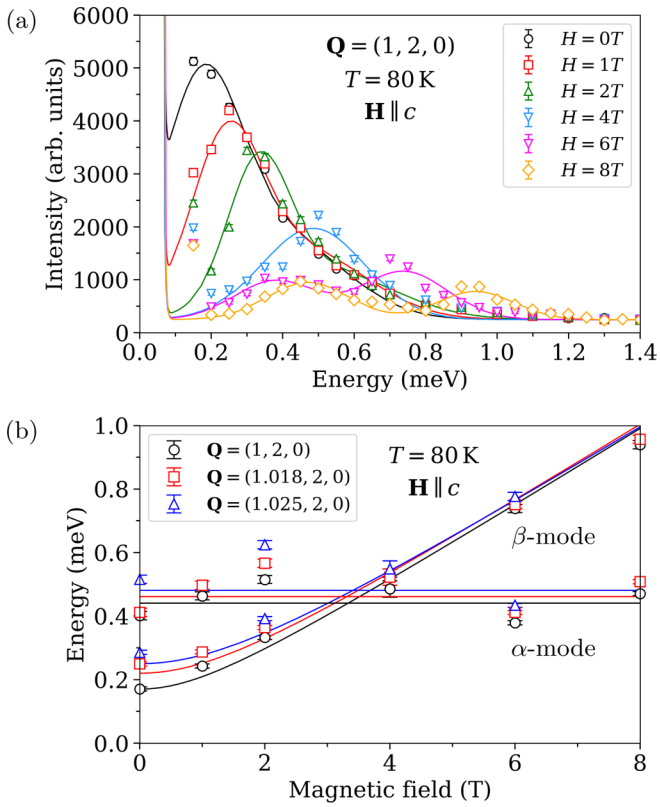

FIG. 4. (a) Inelastic spectra of Mn_5Si_3 for $\mathbf{H} \parallel \hat{\mathbf{c}}$ obtained at $\mathbf{Q} = (1, 2, 0)$ at $T = 80$ K (AFM2 phase) with an unpolarized beam with $k_f = 1.05$ Å^{-1} at IN12. The lines indicate fits with Gaussian functions. (b) Energy of the spin excitations as a function of the external magnetic field at three different Q_h positions at $T = 80$ K (AFM2 phase). Lines are guides for the eyes.

plane (z axis), and the final polarization was analyzed for a scattering process reversing the initial polarization by 180°. The corresponding measurement channels are canonically labeled SF_{xx}, SF_{yy}, and SF_{zz}, where SF stands for "spin flip."

The neutron-scattering double-differential cross sections for the three SF channels are [20]

$$SF_{xx} = \left(\frac{d^2\sigma}{d\Omega dE}\right)^{x}_{SF} \propto BG_{SF} + \langle \delta M_y \rangle + \langle \delta M_z \rangle, \quad (1)$$

$$SF_{yy} = \left(\frac{d^2\sigma}{d\Omega dE}\right)^{y}_{SF} \propto BG_{SF} + \langle \delta M_z \rangle, \quad (2)$$

$$SF_{zz} = \left(\frac{d^2\sigma}{d\Omega dE}\right)^{z}_{SF} \propto BG_{SF} + \langle \delta M_y \rangle, \quad (3)$$

where BG_{SF} is the background (which includes the nuclear spin scattering) and $\langle \delta M_y \rangle$ and $\langle \delta M_z \rangle$ are the measured magnetic fluctuations. Considering that (i) $\mathbf{Q}$ is in the ab plane, (ii) in the AFM2 phase the magnetic moments lie parallel and antiparallel to the b axis, and (iii) spin waves correspond to precession perpendicular to the ordered moment, then in the crystal frame the cross sections become

$$SF_{xx} \propto BG_{SF} + \sin^2\theta \langle \delta M_a \rangle + \langle \delta M_c \rangle, \quad (4)$$

$$SF_{yy} \propto BG_{SF} + \langle \delta M_c \rangle, \quad (5)$$

$$SF_{zz} \propto BG_{SF} + \sin^2\theta \langle \delta M_a \rangle, \quad (6)$$

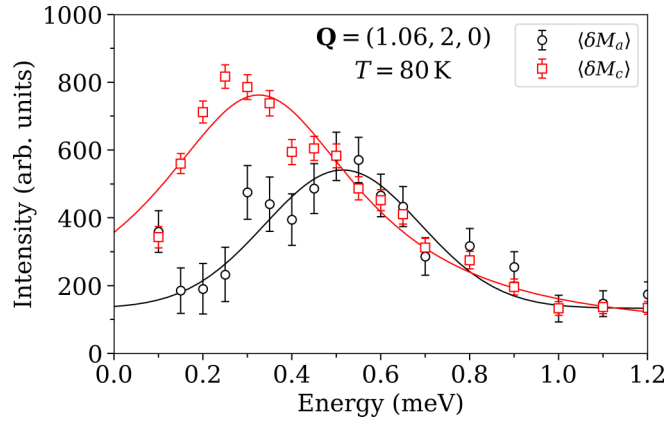

FIG. 5. Subtracted spin-fluctuation spectra $\langle \delta M_a \rangle$ and $\langle \delta M_c \rangle$ of Mn_5Si_3 obtained with ThALES and measured at $\mathbf{Q} = (1.06, 2, 0)$ at $T = 80$ K. The intensity for $\langle \delta M_a \rangle$ was corrected by the factor $\sin^2\theta = 0.545$. The lines indicate fits with Gaussian functions.

where θ is the angle between $\mathbf{Q}$ and the [100] direction and can be calculated by $\theta = \arctan(\frac{Q_k}{Q_h}\frac{a}{b})$.

To gain further insight regarding the polarization dependence of the two magnon modes, E spectra at different $\mathbf{Q}$ positions were collected in the three SF channels at $T = 80$ K. The magnetic fluctuations $\langle \delta M_a \rangle$ and $\langle \delta M_c \rangle$ were extracted by taking the difference of intensities between the different polarization channels. A typical result of such analysis is shown in Fig. 5 at $\mathbf{Q} = (1.06, 2, 0)$ where the intensity for $\langle \delta M_a \rangle$ is corrected by the angle prefactor. The peak positions of the subtracted spin-fluctuation spectra are consistent with the established low-energy magnon dispersion curves obtained from the unpolarized data and shown in Fig. 3(c). Moreover, it is evident that the maximum of intensity in $\langle \delta M_a \rangle$ and in $\langle \delta M_c \rangle$ corresponds to the α mode and the β mode, respectively. This hints that the elliptic polarization of each mode is different and points along different crystal axis.

III. THEORETICAL CALCULATIONS

A. Density functional theory

First-principles calculations were performed to determine the ground-state electronic and magnetic properties of the AFM2 phase of Mn_5Si_3. Our study was based on the atomic structure specified in Ref. [8]. We employed density functional theory (DFT) using the full-potential Korringa-Kohn-Rostoker–Green's-function (KKR-GF) method including spin-orbit coupling, as implemented in the Jülich KKR (JuKKR) code [23], using the local-spin-density approximation [24]. The cutoff for the angular momentum expansion of the scattering problem was set to $l_{max} = 3$. Furthermore, the energy integration was performed in the upper complex energy plane [25] with 30 points in a rectangular path and 5 Matsubara frequencies at a temperature of $T = 473.68$ K, and the Brillouin zone integration was performed with $30 \times 15 \times 30$ k points. The magnetic exchange tensor, which parametrizes the spin Hamiltonian discussed in the following section, was obtained through the *infinitesimal-rotation* method [26,27]. In these calculations, the number of Matsubara frequencies was increased to 10 with $T = 100$ K.

We explored two possible magnetic configurations with self-consistent calculations: the AFM configuration that is shown in Fig. 1 and a ferromagnetic (FM) phase with finite magnetic moments in both Mn1 and Mn2 sites. The AFM was found to be the most energetically favorable with the FM phase being 146 meV per unit cell higher in energy. In the FM phase, the magnetic moments are 2.6 and 1.2 μ_B for the Mn2 and Mn1 sites, respectively, while the Si sites have magnetic moments of 0.1 μ_B antiparallel to those of the manganese sites. For the AFM phase, two-thirds of the Mn2 site carry magnetic moments of 2.4 μ_B, while the other Mn and the Si atoms have no magnetic moment.

Combining the magnetic force theorem with the frozen potential approximation, the magnetocrystalline anisotropy was determined from band energy differences between states with different orientations of the spin magnetic moments. For the AFM phase, we obtained the following energy differences when aligning the magnetic moments along the main crystal axes: $E^a - E^b = 0.12$, $E^c - E^b = 0.09$, and $E^a - E^c = 0.03$ meV per magnetic atom, which indicates that b and c are the first and second preferred axes, respectively, and a is the hard axis.

B. Model Hamiltonian and spin-wave calculation

We mapped the *ab initio* calculations onto a quantum Heisenberg Hamiltonian to study the spin-wave excitations in the adiabatic approximation, which reads as

$$\mathcal{H} = -\sum_{ij} J_{ij}\mathbf{S}_i \cdot \mathbf{S}_j - \sum_{\alpha} k^{\alpha} \sum_{i} \left(S_i^{\alpha}\right)^2. \tag{7}$$

The first term is due to the magnetic exchange interaction, whose coupling is given by J_{ij}. $\mathbf{S}_i$ is the spin, for which we set $S = 1$. The second term accounts for the biaxial magnetocrystalline anisotropy ($\mathcal{H}_{\text{ani}}$) with $k^b = E^a - E^b = 0.12$ meV and $k^c = E^a - E^c = 0.03$ meV, both being positive. From the DFT calculations, we obtained that $k^b > k^c$, which makes b the primary easy axis and c the secondary easy axis. The biaxial anisotropy could also be modeled by a combination of an easy axis along b and an easy-plane (bc plane) anisotropy.

The magnetic exchange interactions were obtained from first-principles calculations for the AFM2 phase. The results for the first few Mn2 pairs as indicated in Fig. 1(a) are $J_1 = -12.23$, $J_2 = -2.16$, $J_3 = 3.98$, and $J_4 = -2.89$ meV. Most interactions, apart from J_3, have AFM character. This indicates that the AFM2 phase is favored by all those pair interactions; that is, within this set of interactions, there is no frustration. J_1, J_2, and J_3 correspond to couplings between magnetic moments in the same $[Mn2]_6$ octahedra. J_1 has the highest value and is the exchange interaction between the spins located on a triangle in the ab plane (distance 2.789 Å). J_2 and J_3 couple spins located on adjacent triangles separated by $c/2$ with distances 2.893 and 4.019 Å, respectively. The exchange interaction J_4 concerns the shortest distance (4.364 Å) between spins located on adjacent $[Mn2]_6$ octahedra.

We employ the linear spin-wave approximation to obtain the spin-wave excitations of the quantum Heisenberg Hamiltonian using the computed magnetic interaction parameters. The spin-wave excitations are the eigenstates of the dynamical matrix associated with the quantum Heisenberg Hamiltonian in Eq. (7), as explained in detail in Ref. [28]. We start by constructing a local coordinate system for every magnetic site with the local z axis coinciding with the classical ground-state spin orientation. In this local frame, we expand the quantum spin operators using the linearized Holstein-Primakoff transformation as $\mathbf{S}_i = (\sqrt{2S}\frac{a_i + a_i^\dagger}{2}, \sqrt{2S}\frac{a_i - a_i^\dagger}{2\mathrm{i}}, S - a_i^\dagger a_i)$, where $a_i^\dagger$ and a_i are bosonic ladder operators [29]. Keeping only terms up to second order in the Holstein-Primakoff bosons, the Hamiltonian can be written as $\mathcal{H} = \mathcal{H}_0 + \mathcal{H}_2$. The $\mathcal{H}_0$ term is a constant corresponding to the classical ground-state energy. The second term

$$\mathcal{H}_2 = -\sum_{\mathbf{k}} \sum_{\mu\nu} \mathbf{a}^\dagger(\mathbf{k}) \mathbf{H}_{\mu\nu}(\mathbf{k}) \mathbf{a}_\nu(\mathbf{k}) \tag{8}$$

contains the quadratic terms of the Holstein-Primakoff bosons describing the spin excitations, where $\mathbf{H}(\mathbf{k})$ is a $2n \times 2n$ matrix and $\mathbf{a}_\mu(\mathbf{k}) = \begin{pmatrix} a_\mu(\mathbf{k}) \\ a_\mu^\dagger(-\mathbf{k}) \end{pmatrix}$ with $a_\mu(\mathbf{k}) = \frac{1}{\sqrt{N}} \sum_m e^{-\mathrm{i}\mathbf{k}\cdot\mathbf{R}_m} a_{m\mu}$. n and N are the number of atoms in the unit and the number of unit cells under periodic Born–von Kármán boundary conditions, respectively. The spin-wave eigenvalues $\omega(\mathbf{k})$ and eigenvectors $|\mathbf{k}\rangle$ are then obtained by a Bogoliubov transformation [30]. This process diagonalizes the system's dynamical matrix $\mathbf{D} = \mathbf{g}\mathcal{H}_2$, where $\mathbf{g}$ is a diagonal matrix containing -1 on its first half and 1 on the second half, while ensuring the bosonic character of the diagonalizing basis. The spin-wave inelastic scattering spectrum is computed with our theory for spin-resolved electron-energy-loss spectroscopy (SREELS) of noncollinear magnets presented in Ref. [28], where we employ time-dependent perturbation theory to describe the interaction between the probing beam and the magnetic excitations. The same theory can be applied with little modification to describe inelastic neutron scattering. This method has been applied to investigate ferromagnetic and antiferromagnetic noncollinear spin textures in Refs. [31–33].

IV. COMPARING EXPERIMENTAL AND THEORETICAL RESULTS

A. Results without an external magnetic field

As already mentioned, the DFT calculations found that the collinear AFM2 phase is more stable than the FM one, in line with the experimental finding that the collinear AFM2 phase is stable in an intermediate temperature range [8]. The AFM2 phase has the peculiarity that one-third of the Mn2 sites and all the Mn1 sites have vanishing ordered magnetic moments, with the main question being whether this is due to a collapse of the local magnetic moment or due to a disordering of their orientation. In the DFT calculations, we considered the collapse scenario, which did not lead to a strong energetic penalty, given that the FM phase was still substantially higher in energy. However, the obtained strong AFM exchange interactions between the Mn2 moments in the $[Mn2]_6$ octahedra (the stacked triangles in Fig. 1) can also lead to a finite-temperature scenario where a third of the Mn2 moments is orientationally disordered, as proposed for Mn_3Pt in Ref. [34]. The DFT calculations can thus also support a hybrid scenario where orientational disorder is mixed with sizable fluctuations of the magnitude of the moments for the Mn2 sites with vanishing ordered moments. Concerning the

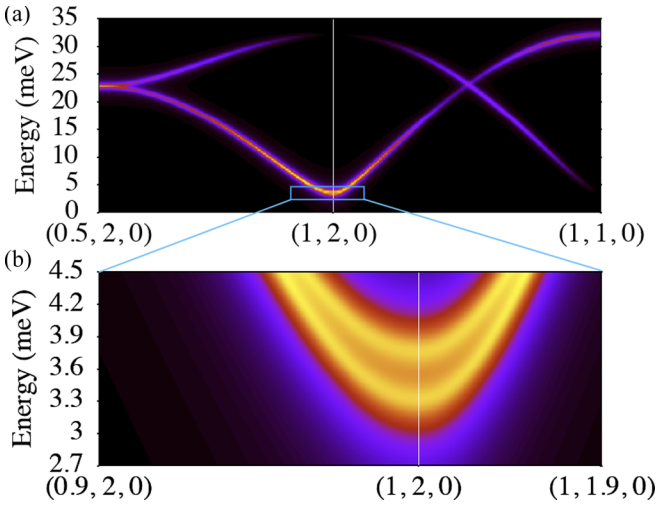

FIG. 6. (a) Theoretical inelastic scattering spectrum for the AFM2 phase of Mn_5Si_3 with parameters obtained from DFT calculations in the absence of an external field. (b) Zooming in on the low-energy regions of the spectrum, a splitting of the spin-wave modes is observed (double spin gap) due to the system's biaxial anisotropy.

Mn1 sites, the DFT calculations suggest that their magnetic moments are unstable on their own and come into existence depending on the Mn2 environment. When this environment is FM, a sizable magnetic moment arises in the Mn1 sites, while if this environment is AFM, the magnetic moment collapses. We conclude that the DFT calculations do not rule out the existence of strong spin fluctuations either on the Mn1 or on the Mn2 sites. Previous experimental work [4] has suggested that the magnetic excitation spectrum of the AFM2 phase consists of propagating spin waves and diffuse spin fluctuations, originating from the presence of magnetic and nonmagnetic Mn sites within this phase, respectively. Further investigation is required to enlighten this phenomenon.

The INS data obtained in the collinear AFM2 phase of Mn_5Si_3 have demonstrated a spin excitation double energy gap for zero field at $\mathbf{Q} = (1, 2, 0)$; see Fig. 4(b). That is, the low-energy spectrum is composed of two excitations of nonvanishing and distinct energies. In a system with uniaxial anisotropy, these two excitations would be degenerate. Using the parameters obtained in our first-principles simulations and given in the previous sections, we calculated the inelastic scattering spectrum for this phase of our material, as seen in Fig. 6(a). In the low-energy region around the Brillouin zone center $\mathbf{G} = (1, 2, 0)$, we observe an energy gap of about 3 meV. However, a closer look reveals the double energy-gap structure, which is due to the second easy-axis anisotropy predicted in our calculations, as demonstrated by Fig. 6(b).

Despite this qualitative agreement, these energy gaps are much higher than those in Fig. 4(b) obtained through the neutron-scattering measurements. We believe that this discrepancy comes from the difficulties associated with modeling the spin-wave spectrum at finite temperature. For example, the computed magnetic moments (2.4 μ_B) are higher than the ones obtained experimentally (1.48 μ_B) [8], which could be explained by the thermal fluctuations of their orientations, which have not been theoretically considered. Possible effects associated with the spin fluctuations of the Mn1 or Mn2 sites are also not taken into account by our model Hamiltonian. Another source of uncertainty is how temperature may affect the magnetic interactions that define the spin-wave excitation spectrum. For instance, the effective magnetic anisotropy energy was found to be strongly temperature dependent in Mn_5Ge_3 [35], the ferromagnetic counterpart of Mn_5Si_3.

To allow a direct comparison between the theoretical spin-wave energies and the experimental data, we rescaled the DFT parameters to match the experimental results. A good agreement was obtained by scaling down uniformly the magnetic exchange interaction and the anisotropy parameters by a factor of 10. For fine-tuning, the second easy-axis anisotropy parameter was adjusted from the scaled DFT value $k^c = 0.003$ meV to $k^c = 0.009$ meV.

B. Results under an external magnetic field

Using the rescaled parameters, we calculated the spin-wave energies as a function of the applied magnetic field to shed light on the observed behavior of the two low-energy magnon modes. To this aim, we included in our model Hamiltonian the Zeeman term,

$$\mathcal{H}_Z = -2\mu_B \sum_i \mathbf{H} \cdot \mathbf{S}_i, \tag{9}$$

to account for an external magnetic field applied along the c and a crystal axes. It is worth mentioning that previous investigations in AFM systems with uniaxial and biaxial anisotropy have described the influence of an external magnetic field in the magnon properties [36,37]. However, the observed behavior from our INS results shown in Fig. 4(b) is not sufficiently covered.

The results of our calculations for an external magnetic field applied along the c crystal axis are shown in Fig. 7(a). We observe that the energy of one mode is insensitive to the magnetic field (α mode), while the energy of the other mode (β mode) increases monotonically for larger fields. Moreover, the β mode is lower in energy than the α mode for zero field, and for increasing field strength they eventually cross, which is in qualitative agreement with the INS data shown in Fig. 4(b). No avoided crossing is observed with our model. At zero field, the energy of the α mode is solely a function of k^b and the magnetic exchange interactions. The energy difference between the two modes is determined by k^c, which is zero for $k^c = 0$. When $k^c = k^b$, the β-mode gap closes. These results are made explicit by our analytical study of a corresponding one-dimensional antiferromagnetic system including nearest-neighbor-only exchange interaction J and a biaxial anisotropy. In the asymptotic limit of $k \ll J$ [38], the energies of two spin-wave modes are $E^\alpha \approx 2S\sqrt{Jk^b}$ and $E^\beta \approx 2S\sqrt{J(k^b - k^c)}$. We note that $k^c > k^b$ represents an unstable situation because the c axis becomes the preferred one but the magnetic moments are aligned along b. If we apply the field along a, the field dependence of these modes inverts, as shown in Fig. 7(b).

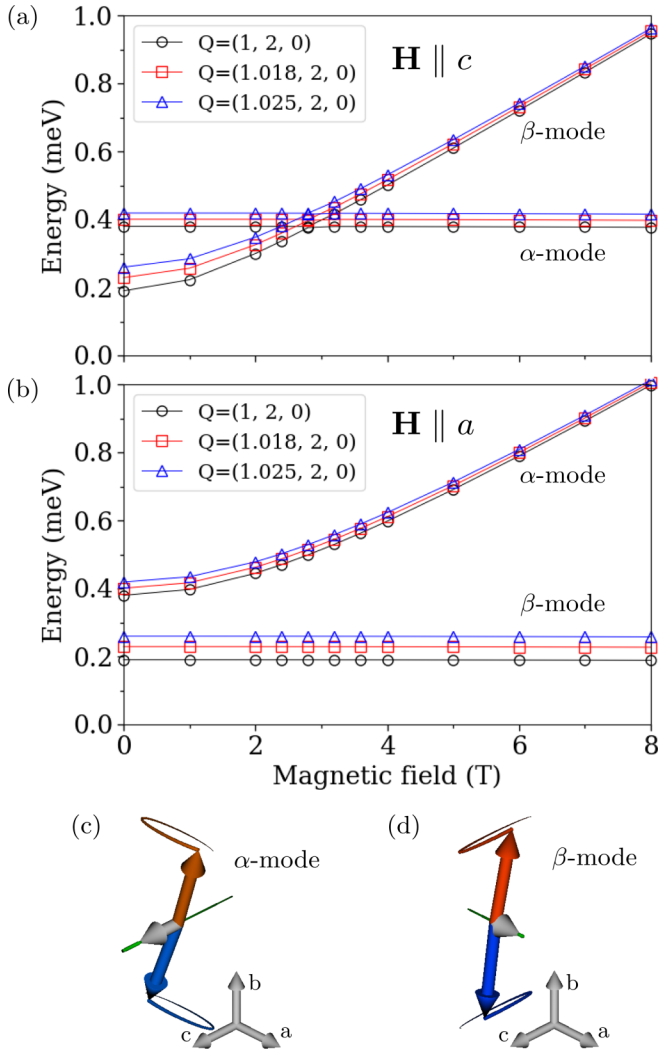

FIG. 7. Adiabatic spin-wave energies of Mn_5Si_3 as a function of the external field. (a) External field applied along the c axis (perpendicular to the preferred axis but parallel to the second anisotropy easy axis). The β mode disperses with the field because it has linear polarization perpendicular to it. Meanwhile, the α mode has linear polarization parallel to the field (along the c axis). (b) External field applied along the a axis (parallel to the hard axis). The field couples with the α mode, which has linear polarization perpendicular to it. In this case, no energy crossing occurs. Lines in (a) and (b) are guides for the eyes. (c) and (d) Precessional dynamics of the spins for biaxial anisotropy and without an external magnetic field for modes α and β, respectively. The red and blue arrows indicate antiparallel spins within a Mn2 triangle precessing around their equilibrium direction (b axis). The central gray arrows represent the dynamics of the net magnetization of the system, which correspond to linear (longitudinal) precessions.

C. Precessional nature of the spin-wave modes

To understand why the two spin-wave modes react so differently to the external magnetic field, we now discuss their precessional nature. For zero field and $k^c = 0$ (i.e., with uniaxial anisotropy), the modes are degenerate as pointed out before. For these modes, the spins have an elliptical precession because in a certain instant of their revolution they are perfectly antiparallel but a quarter of a revolution later they are noncollinear [36]. This noncollinear alignment is unfavored by the exchange interaction, making the precession elliptical. The ellipses describing the precession of each mode have their major axes perpendicular to each other. However, there is no preferred orientation for these major axes as long as the system remains isotropic in the ac plane. Besides, these modes can also be globally characterized by the dynamics of the net magnetization, which is defined by the sum of all spins at each instance in time. For these modes, the net magnetization oscillates linearly along the minor ellipse axis of the corresponding mode, as illustrated by the central gray arrow in Figs. 7(c) and 7(d). These modes are said to be linearly polarized along the oscillation axis of the net magnetization. Furthermore, they have no net angular momentum and can be thought of as longitudinal modes [28].

A preferred direction of the ellipse major axes can be achieved in two ways. Firstly, we can apply a magnetic field perpendicularly to the preferred axis, i.e., $\perp b$ axis. Assuming that the field was applied along c, the α mode becomes linearly polarized along c, and consequently, the β mode is polarized along a. An oscillating net magnetization parallel to the field is not subjected to a torque due to that field. Therefore only the β mode with polarization perpendicular to the magnetic field is affected such that its energy increases with the field.

Secondly, we can introduce a second anisotropy axis perpendicular to the first with weaker strength, let us say along c. The energy of the mode with the major axis of the ellipse along c (β mode) is reduced because the system gains energy when the spins tilt in that direction. The energy of the α mode, which tilts mostly perpendicularly to c, is not much affected. Adding the magnetic field also along c increases the energy of the β mode as before, which eventually leads to the crossing of the energy of the two modes [see Fig. 7(a)]. Figure 7(b) demonstrates that if we apply the magnetic field along a, therefore perpendicular to the linear polarization of the α mode, then it would be the energy of this mode that would increase with the field.

Polarized neutron-scattering experiments around an AFM zone center capture the elliptic polarization of the magnon modes. Therefore the proposed behavior regarding the polarization of the α and β modes is also reflected in the polarized INS spectra shown in Fig. 5. The major axis of the ellipse of the precessional motion of the α mode is along the a axis, and consistently, the intensity of this mode will appear in the subtracted spin-fluctuation spectra obtained from LPA in $\langle \delta M_a \rangle$. Equivalently, the β mode shows maximum intensity in $\langle \delta M_c \rangle$, since the major axis of the precessional motion is along the c axis.

D. Canting of magnetic moments

Polarized single-crystal neutron-diffraction experiments [8] in the AFM2 phase of Mn_5Si_3 showed that the magnetic moments are aligned along the b axis and that there are no components of moments parallel to the c axis. However, a more recent neutron-diffraction study performed on polycrystalline samples [7] suggested a deviation from the perfect collinearity, which is temperature dependent increasing up to

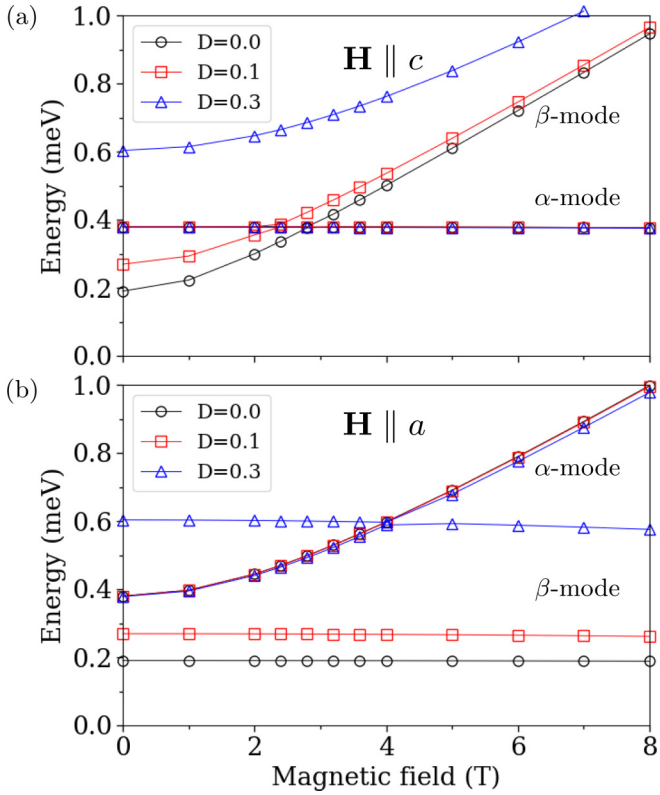

FIG. 8. Effects of the DMI on the spin-wave dispersion of Mn_5Si_3 at $\mathbf{Q} = (1, 2, 0)$. The external field was applied (a) along the c axis (perpendicular to the preferred axis but parallel to the second anisotropy easy axis) and (b) along the a axis (parallel to the hard axis). The DMI increases the energy of the β mode, and its effect on the α mode is almost negligible. $|\mathbf{D}_{ij}| = D$ is in units of meV. Lines are guides for the eyes.

8° near 70 K with respect to the b axis, but with the moments still confined in the ab plane. Such a spin canting could originate from the Dzyaloshinskii-Moriya [39,40] exchange interaction (DMI). To investigate the field dependence of the two modes in the presence of DMI, we included the following term in our model Hamiltonian:

$$\mathcal{H}_{\mathrm{DMI}} = -\sum_{ij} \mathbf{D}_{ij} \cdot (\mathbf{S}_i \times \mathbf{S}_j). \tag{10}$$

The results of the *ab initio* calculation indicated that the DMI is indeed finite and smaller than 10% of the exchange interaction for the Mn2 pair coupled by J_1 where $\mathbf{D}_{ij} || \hat{\mathbf{c}}$. The impact of DMI on the α and β modes for two field directions is shown in Fig. 8. The effect of the DMI in the α mode is almost negligible, independently of the direction of the external magnetic field. In contrast, the DMI causes the β-mode energy to increase. For a field applied along the a axis, the almost flat dispersion of the β mode shifts to higher energies with increasing D, which eventually results in a crossing with the α mode [see the blue curves in Fig. 8(b)]. When the field is applied along the c axis, the increase in energy is accompanied by a change in the "parabolic" dispersion of the β mode, as shown in Fig. 8(a). It is worth noticing that at zero fields, the energy of the α mode is solely given by the exchange interaction and the first anisotropy axis, while the β-mode energy is determined by the DMI in combination with the second anisotropy axis. Based on our results from the INS measurements [see Fig. 4(b)], we can conclude, since a crossing of the two modes is observed for $\mathbf{H} \parallel \hat{\mathbf{c}}$, that the DMI should be very weak in the AFM2 phase of Mn_5Si_3.

V. CONCLUSIONS

We investigated the microscopic magnetic properties of the collinear antiferromagnetic phase of Mn_5Si_3 with inelastic neutron-scattering measurements and density-functional-theory simulations. The measurements have revealed two low-energy spin-wave modes that disperse with the wave vector as expected for gapped antiferromagnetic magnons. The high resolution of the measurements also allowed us to detect the small energy splitting between the two modes of about 0.2 meV. When a magnetic field was applied to the sample along the c axis, the two modes showed a very different response to the field. The energy of the lower-energy mode increased with increasing field, eventually crossing the energy of the other mode, which showed no observable response to the field. These modes were further characterized by polarized neutron-scattering measurements, which showed that their polarization is distinct and likely elliptical, with different major axes for each ellipse. Our first-principles calculations capture the main features observed so far experimentally, namely, the collinear arrangement of the magnetic moments, the coexistence of magnetic and nonmagnetic Mn sites, and the biaxial magnetocrystalline anisotropy. Also, we expanded the existing studies for collinear antiferromagnets with biaxial anisotropy regarding the polarization of the low-energy spin-wave modes and their evolution under the influence of an external magnetic field. Finally, we investigated theoretically the impact of the Dzyaloshinskii-Moriya interaction in the magnon spectrum and its implications depending on the strength of the anisotropy. Our results could find echo in other similar systems where interesting magnonic phenomena occur in the field of antiferromagnetic spintronics.

The neutron data collected at the Institut Laue-Langevin for this paper are available [41–43].

ACKNOWLEDGMENTS

N.B. acknowledges the support of JCNS through the Tasso Springer fellowship. This work was also supported by the Brazilian funding agency CAPES under Project No. 13703/13-7 and the European Research Council (ERC) under the European Union's Horizon 2020 research and innovation program (ERC Consolidator Grant No. 681405-DYNASORE). We gratefully acknowledge the computing time granted by JARA-HPC on the supercomputer JURECA at Forschungszentrum Jülich and by RWTH Aachen University.

[1] V. Baltz, A. Manchon, M. Tsoi, T. Moriyama, T. Ono, and Y. Tserkovnyak, Rev. Mod. Phys. **90**, 015005 (2018).

[2] P. J. Brown, J. B. Forsyth, V. Nunez, and F. Tasset, J. Phys.: Condens. Matter **4**, 10025 (1992).

[3] C. Sürgers, G. Fischer, P. Winkel, and H. v. Löhneysen, Nat. Commun. **5**, 3400 (2014).

[4] N. Biniskos, K. Schmalzl, S. Raymond, S. Petit, P. Steffens, J. Persson, and T. Brückel, Phys. Rev. Lett. **120**, 257205 (2018).

[5] B. Das, B. Balasubramanian, P. Manchanda, P. Mukherjee, R. Skomski, G. C. Hadjipanayis, and D. J. Sellmyer, Nano Lett. **16**, 1132 (2016).

[6] Y. Sun, B. Sun, J. He, G. Yang, and C. Wang, Nat. Commun. **11**, 647 (2020).

[7] M. Gottschilch, O. Gourdon, J. Persson, C. de la Cruz, V. Petricek, and T. Brueckel, J. Mater. Chem. **22**, 15275 (2012).

[8] P. J. Brown and J. B. Forsyth, J. Phys.: Condens. Matter **7**, 7619 (1995).

[9] C. Sürgers, T. Wolf, P. Adelmann, W. Kittler, G. Fischer, and H. v. Löhneysen, Sci. Rep. **7**, 42982 (2017).

[10] L. Vinokurova, V. Ivanov, E. Kulatov, and A. Vlasov, J. Magn. Magn. Mater. **90–91**, 121 (1990).

[11] R. F. Luccas, G. Sánchez-Santolino, A. Correa-Orellana, F. J. Mompean, M. García-Hernández, and H. Suderow, J. Magn. Magn. Mater. **489**, 165451 (2019).

[12] S. C. Das, K. Mandal, P. Dutta, S. Pramanick, and S. Chatterjee, Phys. Rev. B **100**, 024409 (2019).

[13] M. R. Silva, P. J. Brown, and J. B. Forsyth, J. Phys.: Condens. Matter **14**, 8707 (2002).

[14] H. Al-Kanani and J. Booth, J. Magn. Magn. Mater. **140–144**, 1539 (1995).

[15] A. Irizawa, A. Yamasaki, M. Okazaki, S. Kasai, A. Sekiyama, S. Imada, S. Suga, E. Kulatov, H. Ohta, and T. Nanba, Solid State Commun. **124**, 1 (2002).

[16] C. Sürgers, W. Kittler, T. Wolf, and H. v. Löhneysen, AIP Adv. **6**, 055604 (2016).

[17] D. Songlin, O. Tegus, E. Brück, J. C. P. Klaasse, F. R. de Boer, and K. H. J. Buschow, J. Alloys Compd. **334**, 249 (2002).

[18] K. Schmalzl, W. Schmidt, S. Raymond, H. Feilbach, C. Mounier, B. Vettard, and T. Brückel, Nucl. Instrum. Methods Phys. Res., Sect. A **819**, 89 (2016).

[19] L. P. Regnault, B. Geffray, P. Fouilloux, B. Longuet, F. Mantegazza, F. Tasset, E. Lelièvre-Berna, S. Pujol, E. Bourgeat-Lami, N. Kernavanois, M. Thomas, and Y. Gibert, Phys. B (Amsterdam) **350**, E811 (2004).

[20] *Neutron Scattering from Magnetic Materials*, 1st ed., edited by T. Chatterji (Elsevier, Amsterdam, 2006).

[21] In this paper we use the orthorhombic coordinate system, and the scattering vector $\mathbf{Q}$ is expressed in Cartesian coordinates $\mathbf{Q} = (Q_h, Q_k, Q_l)$ given in reciprocal lattice units (r.l.u.). The wave vector $\mathbf{q}$ is related to the momentum transfer through $\hbar\mathbf{Q} = \hbar\mathbf{G} + \hbar\mathbf{q}$, where $\mathbf{G}$ is a Brillouin zone center and $\mathbf{G} = (h, k, l)$.

[22] S. Ibuka, S. Itoh, T. Yokoo, and Y. Endoh, Phys. Rev. B **95**, 224406 (2017).

[23] N. Papanikolaou, R. Zeller, and P. H. Dederichs, J. Phys.: Condens. Matter **14**, 2799 (2002).

[24] S. Vosko, L. Wilk, and M. Nusair, Can. J. Phys. **58**, 1200 (1980).

[25] K. Wildberger, P. Lang, R. Zeller, and P. H. Dederichs, Phys. Rev. B **52**, 11502 (1995).

[26] A. I. Liechtenstein, M. I. Katsnelson, V. P. Antropov, and V. A. Gubanov, J. Magn. Magn. Mater. **67**, 65 (1987).

[27] H. Ebert and S. Mankovsky, Phys. Rev. B **79**, 045209 (2009).

[28] F. J. dos Santos, M. dos Santos Dias, F. S. M. Guimarães, J. Bouaziz, and S. Lounis, Phys. Rev. B **97**, 024431 (2018).

[29] T. Holstein and H. Primakoff, Phys. Rev. **58**, 1098 (1940).

[30] N. N. Bogoljubov, Nuovo Cimento **7**, 794 (1958).

[31] F. J. dos Santos, M. dos Santos Dias, and S. Lounis, Phys. Rev. B **102**, 104401 (2020).

[32] F. J. dos Santos, M. dos Santos Dias, and S. Lounis, Phys. Rev. B **102**, 104436 (2020).

[33] F. J. dos Santos, M. dos Santos Dias, and S. Lounis, Phys. Rev. B **95**, 134408 (2017).

[34] E. Mendive-Tapia and J. B. Staunton, Phys. Rev. B **99**, 144424 (2019).

[35] N. Maraytta, J. Voigt, C. Salazar Mejía, K. Friese, Y. Skourski, J. Perßon, S. M. Salman, and T. Brückel, J. Appl. Phys. (Melville, NY) **128**, 103903 (2020).

[36] F. Keffer and C. Kittel, Phys. Rev. **85**, 329 (1952).

[37] S. M. Rezende, A. Azevedo, and R. L. Rodríguez-Suárez, J. Appl. Phys. (Melville, NY) **126**, 151101 (2019).

[38] F. J. dos Santos, First-principles study of collective spin excitations in noncollinear magnets, Ph.D. thesis, Forschungszentrum Jülich, 2020.

[39] I. Dzyaloshinsky, Phys. Chem. Solids **4**, 241 (1958).

[40] T. Moriya, Phys. Rev. **120**, 91 (1960).

[41] https://doi.ill.fr/10.5291/ILL-DATA.CRG-2331.

[42] https://doi.ill.fr/10.5291/ILL-DATA.CRG-2620.

[43] https://doi.ill.fr/10.5291/ILL-DATA.4-01-1618.